atmosphere

MDPI

Article

Assessment of Radon and Naturally Occurring Radionuclides in the Vredefort Meteorite Crater in South Africa

Rikus Le Roux * and Jacques Bezuidenhout

Faculty of Military Science, Stellenbosch University, Saldanha 7395, South Africa; jb@sun.ac.za
* Correspondence: rikusr@sun.ac.za

Abstract: The concentric impact rings of the Vredefort Crater contain rocks with elevated uranium concentrations resulting from the geological signature of a meteoric impact. The decay of this uranium was estimated to lead to elevated indoor radon concentrations in the Crater, but such a study has never been carried out. This study explores the relationship between the natural radionuclides found in the geology of the Vredefort Crater and indoor radon concentrations. This was achieved through soil sampling and radionuclide surveys conducted on three impact rings, supplemented by indoor radon measurements in dwellings found in the area. In situ measurements revealed that one impact ring had higher-than-average uranium concentrations at 50 Bq/kg. Surprisingly, the measured indoor radon levels were lower than expected (113 Bq/m^3). These measurements were taken during the COVID-19 pandemic and colder months, conditions that would typically result in elevated indoor radon levels. Soil samples indicated uranium activity of 30 Bq/kg, comparable to the world average of 35 Bq/kg. However, defunct mine tunnels in the area exhibited elevated radon concentrations, averaging 364 Bq/m^3. The disparity between expected and measured indoor radon levels was attributed to the composition of surficial deposits, bedrock, and architectural features of the dwellings preventing radon accumulation.

Keywords: naturally occurring radionuclides; uranium; radon; meteorite impact; geology; South Africa

Citation: Le Roux, R.; Bezuidenhout, J. Assessment of Radon and Naturally Occurring Radionuclides in the Vredefort Meteorite Crater in South Africa. *Atmosphere* **2023**, *14*, 1826. https://doi.org/10.3390/atmos14121826

Academic Editors: Qiuju Guo and Miroslaw Janik

Received: 6 November 2023
Revised: 27 November 2023
Accepted: 12 December 2023
Published: 15 December 2023

Correction Statement: This article has been republished with a minor change. The change does not affect the scientific content of the article and further details are available within the backmatter of the website version of this article.

1. Introduction

Radon, a colorless and odorless radioactive gas, is a ubiquitous environmental hazard that poses a significant risk to human health. Originating from the natural decay of uranium (^{238}U) in soil, rock, and water, radon can accumulate in enclosed spaces, such as homes and workplaces, reaching concentrations that may lead to adverse health effects. The World Health Organization (WHO) considers radon to be the second largest contributor to lung cancer [1]. Recognizing the importance of understanding and mitigating the accumulation of this gas inside dwellings, numerous countries around the world have undertaken comprehensive radon surveys to assess the extent of radon exposure in their respective regions [2–4].

In 2018, the South African National Nuclear Regulator (NNR) initiated a project call to design a national indoor survey for the country. In an attempt to identify potential radon hotspots for targeted sampling, the geology and climate of South Africa was studied [5,6] and combined with a model [7] to estimate the indoor radon concentrations based on the uranium content of the geological formations.

Uranium (^{238}U), a primordial radionuclide and a common constituent in many geological formations, undergoes a series of radioactive decays through alpha, beta, and gamma radiation, ultimately leading to the formation of radon (^{222}Rn). During this decay, radioactive progenies such as thorium (^{234}Th), uranium (^{234}U), and radium (^{226}Ra) are produced. Radon-222 (^{222}Rn) is the most stable nuclide of radon. It is the immediate decay product of ^{226}Ra and contributes to the exposure to indoor radon [8]. This gaseous nuclide

has a half-life of 3.82 days, after which it undergoes further decay, eventually reaching the stable nuclide of lead (^{206}Pb). When inhaled, it is this decay of radon gas that can be carcinogenic.

In addition to ^{238}U, other primordial radionuclides are commonly found in Earth's geology. These include thorium (^{232}Th) and potassium (^{40}K), each with its own decay chain. It was the concentrations of these primordial natural radionuclides in the geology that were used by one of the current authors (Bezuidenhout) to compile geographic information systems (GIS) maps, highlighting and identifying potential areas of high indoor radon accumulation [5].

Amongst the key areas that Bezuidenhout identified was the Vredefort Crater, the largest and oldest verified impact crater on the planet, which is located around 120 km southwest of Johannesburg, South Africa. Due to the meteoric impact, this area is rich in unique geological formations [9] and various studies have been performed in this area [10–12].

Though a stable isotope study has been performed in this area [13], no radiometric or indoor radon study has been done. This study, therefore, set out to verify Bezuidenhout's estimation of high indoor radon concentrations in the Vredefort Crater. This was done by first assessing the natural radionuclide concentrations found in the area through in situ measurements, followed by indoor radon measurements. The in situ measurements focused predominantly on thorium and uranium due to radon gas being part of their decay chain. Gamma-ray spectroscopy was performed, and since ^{238}U and ^{232}Th primarily emit alpha particles in their initial decay processes, this process had to consider the daughter nuclides from the decay. Also included in the study was ^{40}K, due to its abundance in nature, even though it does not contribute towards the accumulation of radon through its decay.

2. The Vredefort Crater

The Vredefort Crater was formed approximately 2023 million years ago by a meteorite impact. Geophysical modeling estimates the diameter of the original impact structure to be 300 km [14]. Most of the surface features of the impact crater have eroded away [15], leaving only the exposed deep structure of the impact [14]. This structure, which represents only the central uplift of the crater, is known as the Vredefort Dome and is almost 60 km in diameter [16]. The core of this Dome was uplifted from the mid-crustal by the impact [17]. The core and the impact rings consist of rocks that contain comparatively high concentrations of naturally occurring radionuclides [7]. For these reasons, the Vredefort Dome is an excellent location for monitoring naturally occurring radionuclides and their offspring like radon and thoron.

The northwestern part of the Vredefort Dome was proclaimed a Serial Natural World Heritage Property in 2005. This site covers an area of about 300 km^2 and is surrounded by a 5 km buffer zone to safeguard the site from external development pressures [18]. Figure 1 shows a photo of two hills in the Heritage Site that surrounds the core of the Dome. The site contains some of the most significant geological formations illustrating the structure of the meteorite impact. This area is, therefore, ideal for evaluating Bezuidenhout's prediction of elevated indoor radon concentrations by investigating the relationship between the naturally occurring radionuclides and radon and thoron. Thoron, however, has a very short half-life, which complicates accurate indoor measurements [19].

Figure 1. A photo of two hills from different geological units (Dome rings) that were measured during the in situ survey.

3. Geological Setting

The interior of the Vredefort meteor crater is dominated by gneisses that belong to the Archean basement granite gneiss (R3 in Figure 2), with minor amphibolites and is cut by a few granophyre dykes (impact melt) and local networks of pseudotachylitic breccia [20]. A crustal rebound following the impact raised deeper mid-crustal granitoids (Z4 in Figure 2) into the core of the crater [16]. The dominant Archean basement comprises trondhjemitic–granodioritic gneisses cut by younger granites (pink units in Figure 2) [21].

The basement interior of the Vredefort Dome is rimmed by concentric rings of steeply dipping volcaniclastic strata that were uplifted and tilted by the impact, around the more exhumed dome interior. This volcaniclastic collar is particularly well exposed across the northern to north-western parts of the dome structure, while southern to southeastern parts are mostly buried below younger Karoo formations (Pe in Figure 2) [22]. The impacted volcaniclastic collar is made up of stratigraphically younger Witwatersrand, Ventersdorp to Transvaal Supergroups [23]. The predominantly clastic Witwatersrand Supergroup contains conglomerates with distinctive quartzite pebbles, while the more volcanic Ventersdorp Supergroup is made up of basalts and andesites, and the Transvaal Supergroup is highly dolomitic above its clastic base [24].

The Witwatersrand Supergroup is distinguished into six subgroups and the study was conducted across the outer/upper two of these subgroups, as well as the overlying Ventersdorp Supergroup. The area covered is indicated by the red rectangle in Figure 2. The inner/lower Johannesburg subgroup comprises conglomerates, quartzites, shales, and rare volcanic beds, while the outer Turffontein subgroup comprises quartzites and subordinate conglomerates.

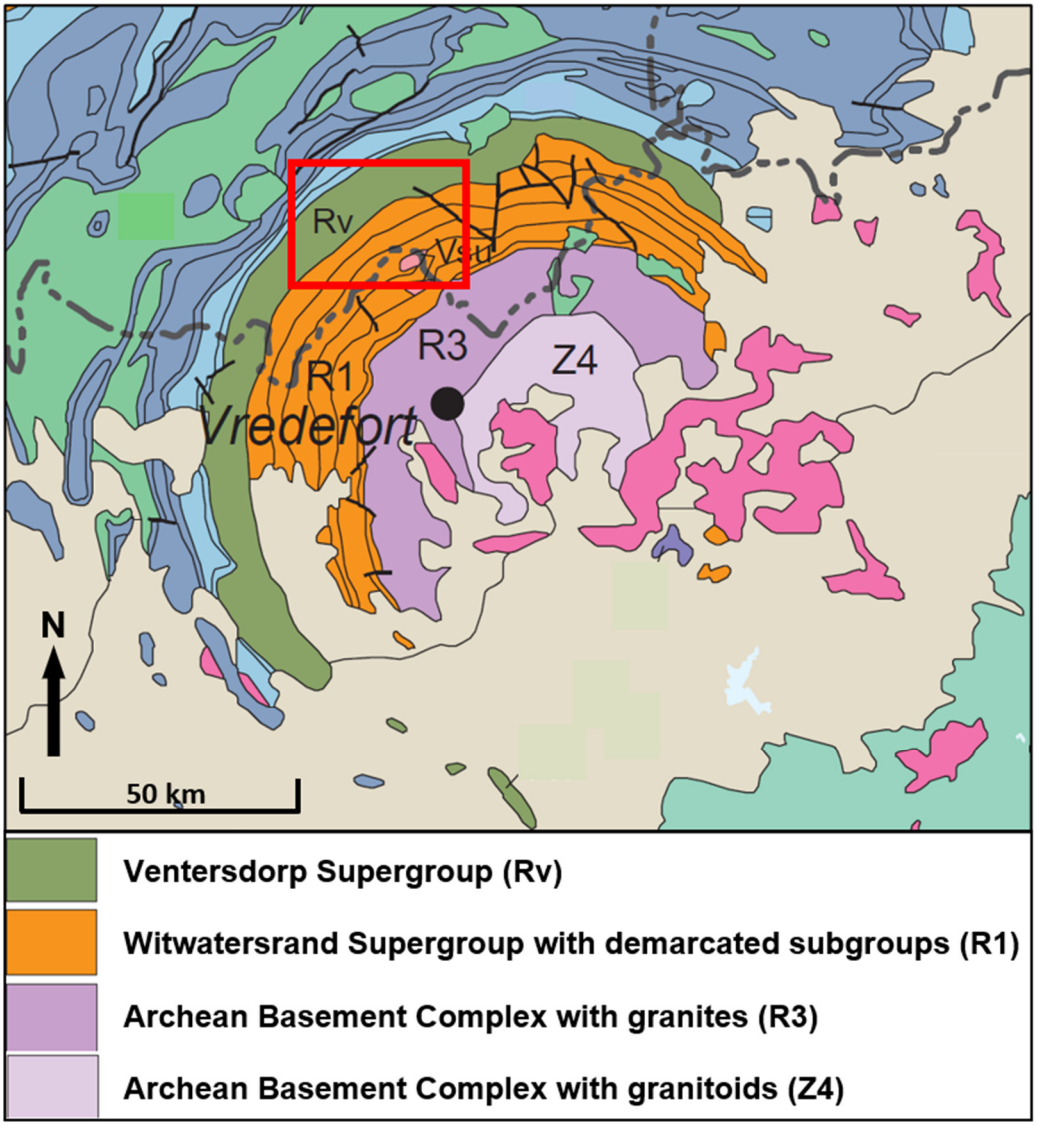

Figure 2. A geological map of the Vredefort meteor impact crater. The town of Vredefort is shown as a black dot and the study area is indicated by a red rectangle. (Modified from the RSA geological map 1997 by the Council of Geoscience of South Africa, obtained from https://www.geoscience.org.za, assessed on 1 October 2023).

4. Radionuclide Measurements and Assessment

4.1. In Situ Survey of Naturally Occurring Radionuclides

During the in situ survey, a custom-designed Gamma Ray In Situ Portable Instrument (GISPI) was carried in a backpack and transported by vehicle. The methods used were similar to those described by Bezuidenhout [25]. The GISPI consists of a 3 × 3 NaI(Tl) scintillation detector, a scintiSPEC® MCA (http://gs.flir.com/, accessed on 20 December 2014), and a rugged laptop with an onboard GPS [26]. Regions of Interest (ROIs) in the recorded in situ spectra were used to extract the concentrations of the various naturally occurring nuclides. The following ROIs were associated with the nuclides, 238.6 keV, 351.9 keV, 1460.8 keV, 1764.5 keV, and 2614.5 keV for ^{232}Th, ^{238}U, ^{40}K, ^{238}U, and ^{232}Th, respectively.

The GISPI was managed by real-time analysis software that controlled the system and automatically gathered the data. Measurements were taken at regular intervals of 15 s and linked with corresponding geographical coordinates for further visualization. The nuclide concentrations that were extracted were then used to produce graded point

overlays on maps and images. The results are shown in Section 5. The energy and efficiency of the GISPI were properly calibrated before the survey. The ^{40}K gamma emission, which is generally very significant in natural spectra, was used as an active stabilization peak in the winTMCA32 software of the scintiSPEC®, which then automatically corrected for energy drift.

Two field surveys were conducted inside the accessible part of the Vredefort Dome to comprehensively study a wide range of geological units. The selection of the northeastern portion of the Vredefort Dome was based on its location inside the Natural World Heritage site. A portion of the region was not accessible through transportation, necessitating a survey conducted on foot while carrying the detecting equipment. The surveys covered four geological units: the Venterdorp Supergroup, the Turffontein and Johannesburg Subgroups, and alluvial sediment.

4.2. Sample Measurements, Analyses, and Mapping

The laboratory gamma-ray spectra were recorded using a NaI(Tl) detector with dimensions of 7.62 cm × 7.62 cm, which was connected to a scintiSPEC® Multi-Channel Analyzer (http://gs.flir.com/, assessed on 20 December 2014). The scintiSPEC® Multi-Channel Analyzer, manufactured by ICX Technologies, Solingen, Germany, has a USB interface that serves the dual purpose of providing operating voltage and facilitating signal transfer. The management of system settings and spectrum acquisition were managed using winTMCA32 software, developed by ICX Technologies, which had 1024 channels. The detector was shielded in a lead castle 15 cm in thickness, resulting in a significant reduction and smoothing of the background radiation. Polypropylene pill containers were used for the storage of both the laboratory standards and the sample materials. A volume of 100 cm^3 was used, and the masses of the samples varied between 0.078 kg and 0.147 kg. As laboratory standards for the efficiency and energy calibrations, three IAEA-approved reference materials containing ^{40}K, ^{238}U, and ^{232}Th nuclides were utilized. The laboratory analyses were conducted according to the procedure recommended by Bezuidenhout [27]. Three counting ROIs were selected and associated with the three naturally occurring nuclides. These were 1460.8 keV, 1764.5 keV, and 2614.5 keV for ^{40}K, ^{238}U, and ^{232}Th, respectively.

All the activity concentrations were calculated in Bq/kg. These activity concentrations were then imported, plotted, and interpolated by QGIS software, and overlaid on Google Earth images and geological maps. The data of the geological units in South Africa were obtained from the Council of Geoscience of South Africa (https://www.geoscience.org.za, assessed on 1 October 2023). IAEA mapping standards prescribing red for potassium, blue for uranium, and green for thorium were applied to each image. Nonetheless, the investigation was limited to uranium and thorium in relation to radon and thoron, respectively. Details of the obtained results are given in the next section.

4.3. Indoor Radon Assessment

In order to assess the radon offspring from the natural nuclides found in the Vredefort impact crater's surrounding geology, measurements were performed during winter in 26 locations in the Ventersdorp (Rv) and Witwatersrand (R1) Supergroups indicated in Figure 2. Four guest farms were identified that are located in these formations. The locations of the farms are indicated in Figure 3. Due to the COVID-19 pandemic, guest farm 2 remained non-operational. Unlike the farmhouse and residences of the farm workers, the chalets remained unoccupied. Guest farms 1, 3, and 4 have resumed limited operation. Electret ion chambers (EICs), called E-PERM®, from Rad-Elec Inc., Frederick, MD, USA, were placed in the living rooms of the chalets, residences of farmworkers, and farmhouses on the farms. The chambers were placed more than 1 m above the floor and 1 m clear of any windows, doors, or walls. Preference was given to dwellings that can remain closed for the duration of the measurements to mitigate the effect of ventilation. In the case of occupied dwellings, occupants were left to continue their normal routine, thereby determining their

typical exposure to radon gas. However, due to the relatively cold climate during the measurement period, limited indoor ventilation was nonetheless expected.

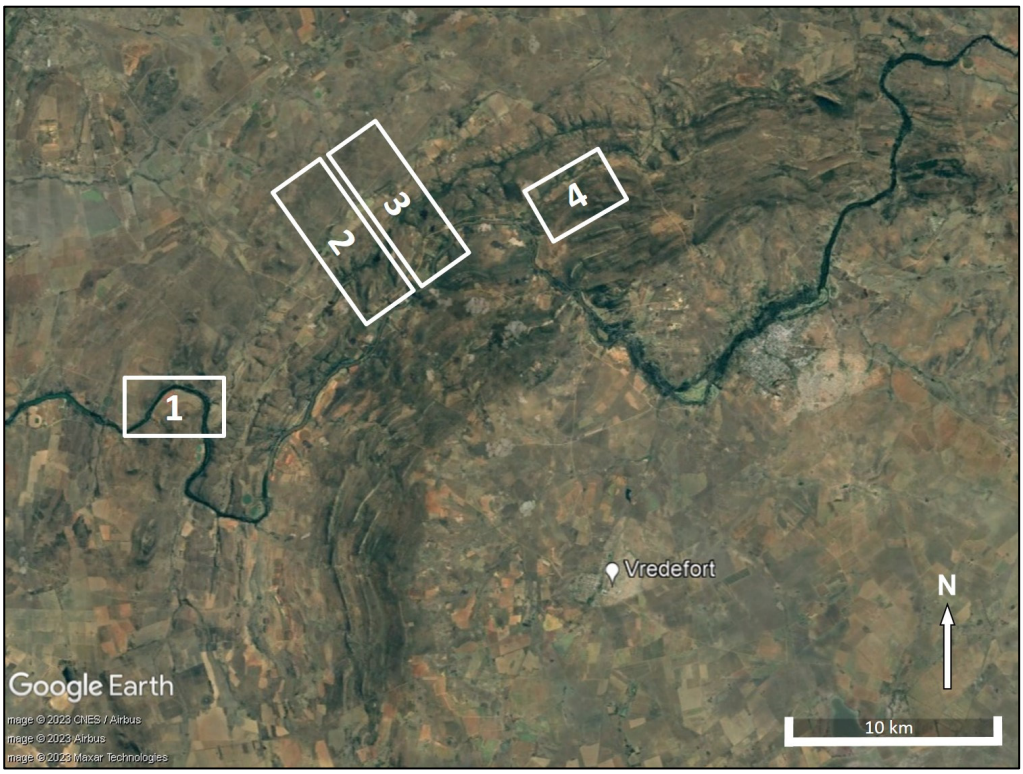

Figure 3. A Google Earth image showing the location of the four guest farms, indicated by the numbered regions, where indoor radon measurements were carried out.

To accumulate the radon gas, measurements were done for an average of 3.5 days. The initial and final potential of each electret was measured using a surface potential electret voltage reader (SPER) reader, also from Rad-Elec Inc., and the difference in potential over the measurement period was used to calculate the airborne radon concentration using Equation (1)

$$RnC = \frac{\left(V_i - V_f\right)}{(T)(CF)} - BG \quad (1)$$

where RnC represents the indoor radon concentration, V_i and V_f are the initial and final electret potentials respectively, T is the deployment time in hours, CF is a linearization coefficient [28], and BG is the radon concentration equivalent of the natural gamma (γ) radiation background. A background radiation correction was made by assuming a typical gamma radiation of 32 Bq/m^3 [29].

The sedimentology of the Vredefort sub-basin is similar, geometrically and structurally, to other sub-basins within the Witwatersrand Basin such as the Klerksdorp and West Rand Goldfields. Unusually coarse conglomerates from the upper part of the Witwatersrand Supergroup around the Vredefort Dome were first reported by Mellor [30] and described in more detail by Nel [31]. These conglomerates, which occur in the Kimberley Formation of the Turffontein Subgroup, were first mined in the Vredefort Dome in 1886, but due to unsatisfactory results, operations were largely discontinued in around 1911 [32]. Remnants of these mining activities can still be found in the area in the form of mining tunnels.

Radon emission is strongly influenced by the geological characteristics of the bedrock. To investigate the contribution of the geology to the radon concentration measured indoors, EICs were also placed in five defunct mine tunnels found on farm 3. Also, 20 ground samples were taken for radiometric analysis in a lead castle with a 3 × 3 NaI(Tl) scintillation detector.

5. Results and Discussion

Two in situ surveys were conducted in the northeastern part of the Vredefort Dome, one using a rucksack to carry the detector system and the other using a vehicle to transport the detector system. The on-foot and on-vehicle surveys, respectively, covered two and four geological units. Figures 4 and 5 demonstrate that the concentrations of uranium and thorium are considerably higher in the two subgroups of the Witwatersrand Supergroup (Turffontein and Johannesburg subgroups) than in the Venterdorp Supergroup. Parts of the Turffontein unit demonstrate high concentrations (greater than 50 Bq/kg), which may be associated with shale beds and conglomerates.

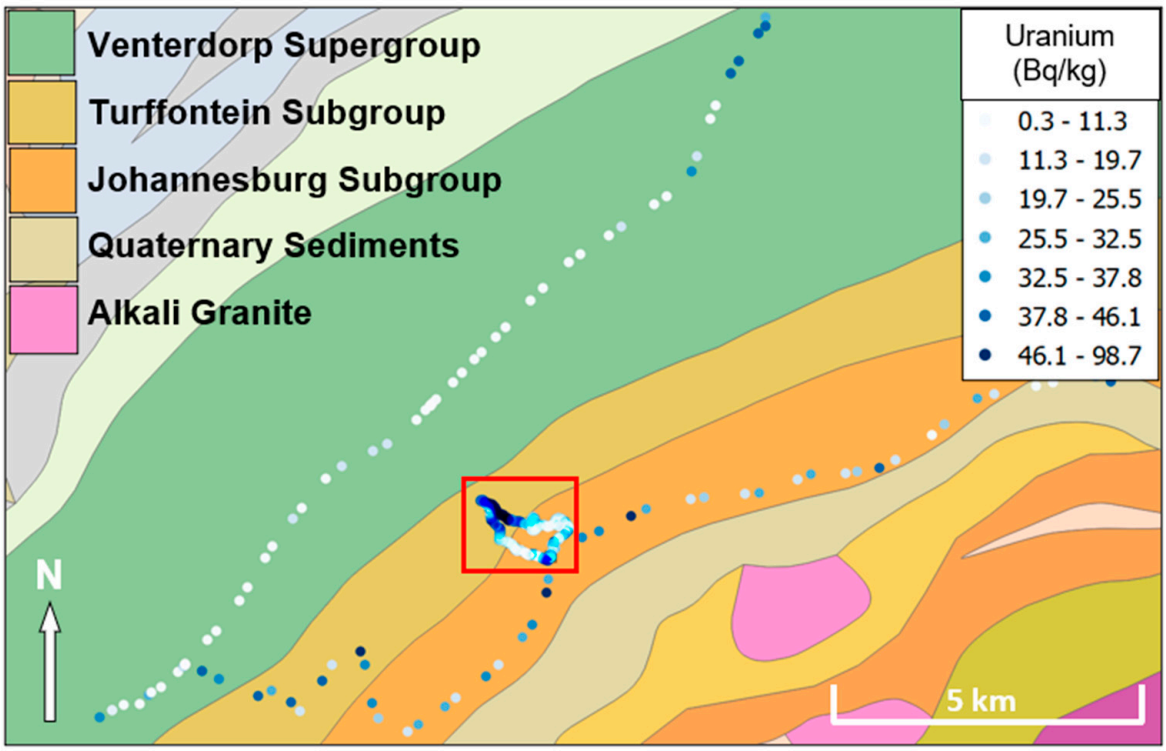

Figure 4. A geological map of the northeastern section of the Vredefort impact crater with a color-graded overlay that shows the in situ and on-foot measured uranium concentrations (Bq/kg). The red square demarcates the part of the survey that was done on foot (Modified from the RSA geological map, 1997, by the Council of Geoscience of South Africa, obtained from https://www.geoscience.org.za, assessed on 1 October 2023).

Figure 5 depicts a clear distinction between the thorium concentrations of the Turffontein geological unit and those of the adjacent units. This is evident in both the vehicle survey and the survey conducted on foot. The increased thorium concentration in a river valley in the far north of the surveyed area can be attributed to alluvial deposits in that region.

As shown in Figure 6, the uranium concentrations in the area that was measured on foot indicate a distinct increase in the part of the route that runs on the Turffontein subgroup. The highest values in this unit are in a riverbed that flows down the mountain. Again, this suggests that the alluvial sediment in this area might be responsible for the high concentrations of uranium and thorium.

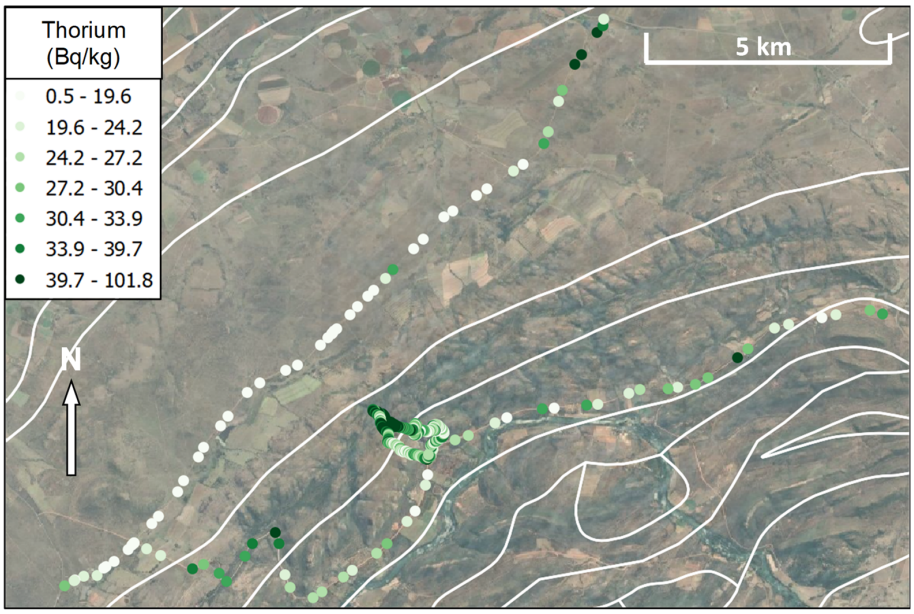

Figure 5. A Google Earth image of the northeastern section of the Vredefort impact crater with a color-graded overlay that displays measured thorium concentrations (Bq/kg) with the borders of geological units, which are indicated as white lines.

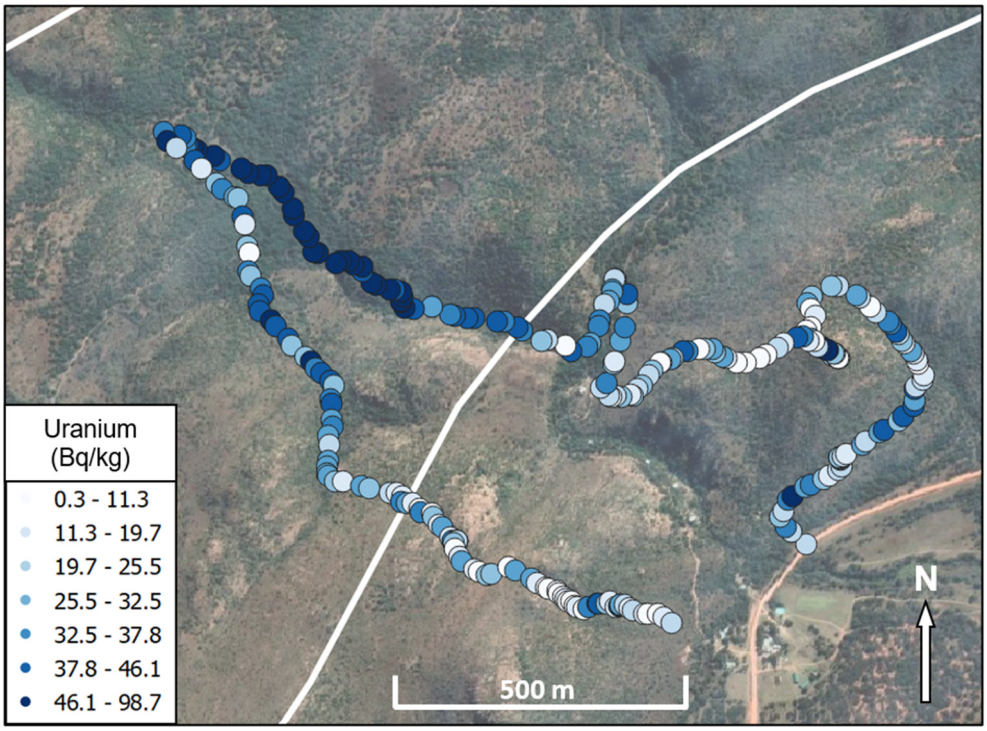

Figure 6. A Google Earth image showing measurements that were done on foot covering two geological units of the Witwatersrand Supergroup. A color-graded overlay displays the measured uranium concentrations (Bq/kg) and the borders of geological units are indicated as white lines. This image presents an excerpt of the measurements shown in Figure 4, illustrating the characteristics of the terrain.

The in situ measurements on foot crossed two ridges that are part of the two rings of the Dome comprising the Johannesburg and Turffontein subgroups, respectively. Figure 1 displays a photograph of ridges 1 and 2 from left to right. Ridge 1 was traversed, then ridge 2, whereafter ridge 1 was crossed again on the way back. Figure 7 shows an elevation

graph with the uranium concentrations superimposed. The upper portions of the first ridge exhibit low uranium concentrations, which correspond with the presence of quartzite in the underlying geology. In contrast, areas surrounding alluvial cavities have elevated uranium concentrations.

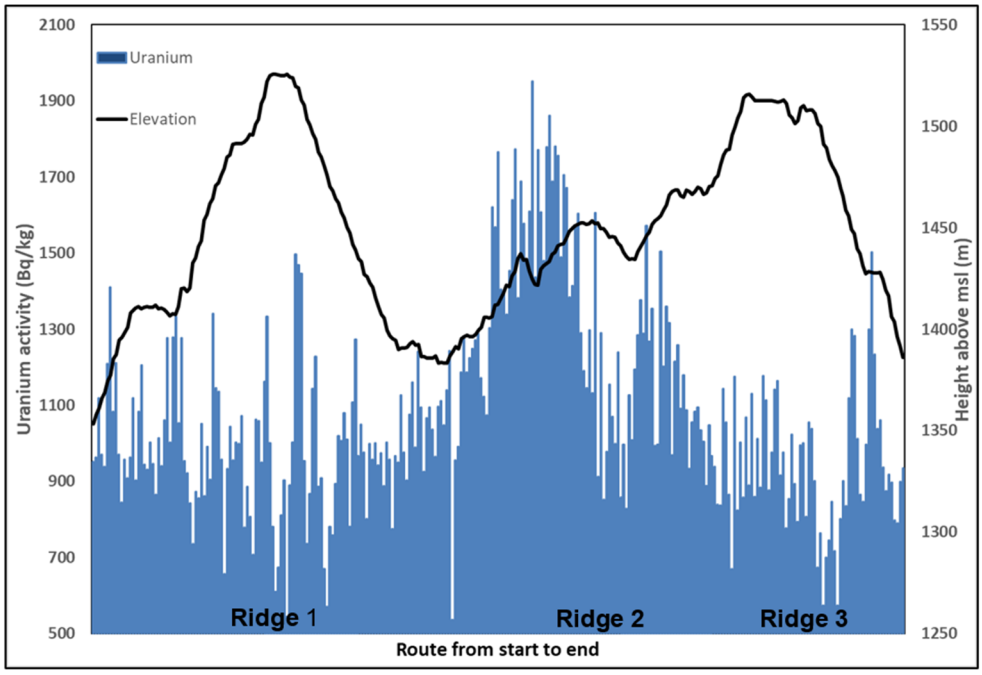

Figure 7. An elevation graph with an overlay of the uranium concentrations of the measurements that were done on foot. The uranium activity (Bq/kg) is scaled by a factor of 10 for visual purposes.

Figure 8 indicates the locations where the indoor radon measurements were conducted along with an interval grouping for the calculations. Since South Africa does not have a radon reference level at the time of writing, the intervals exceeding 100 Bq/m^3 were based on typical radon reference levels used throughout the world, which range from 100 Bq/m^3 to 300 Bq/m^3 [1,33]. The results from the indoor radon measurements are given in Figure 9 and compared in Table 1. An average indoor radon concentration of 113 Bq/m^3 was measured, with 11 measurements exceeding 100 Bq/m^3. Two measurements exceeded 200 Bq/m^3, with the highest measured radon concentration being 280 Bq/m^3.

Table 1. The calculated indoor radon concentration along with the average concentrations for the four farms.

Area	Sample	Calculated Rn Concentration (Bq/m^3)	Average Rn Concentration (Bq/m^3)
Farm 1	1	156.95	126.10
	2	95.24	
Farm 2	1	64.24	104.14
	2	61.98	
	3	57.92	
	4	185.46	
	5	99.32	
	6	155.89	

Table 1. *Cont.*

Area	Sample	Calculated Rn Concentration (Bq/m^3)	Average Rn Concentration (Bq/m^3)
Farm 3	1	128.21	110.15
	2	130.42	
	3	88.03	
	4	177.97	
	5	233.24	
	6	55.44	
	7	80.24	
	8	49.40	
	9	91.56	
	10	101.05	
	11	52.66	
	12	67.49	
	13	176.18	
Farm 4	1	280.45	124.95
	2	112.31	
	3	87.35	
	4	87.04	
	5	57.60	
Mines	1	299.18	364.22
	3	248.46	
	4	710.86	
	5	198.38	

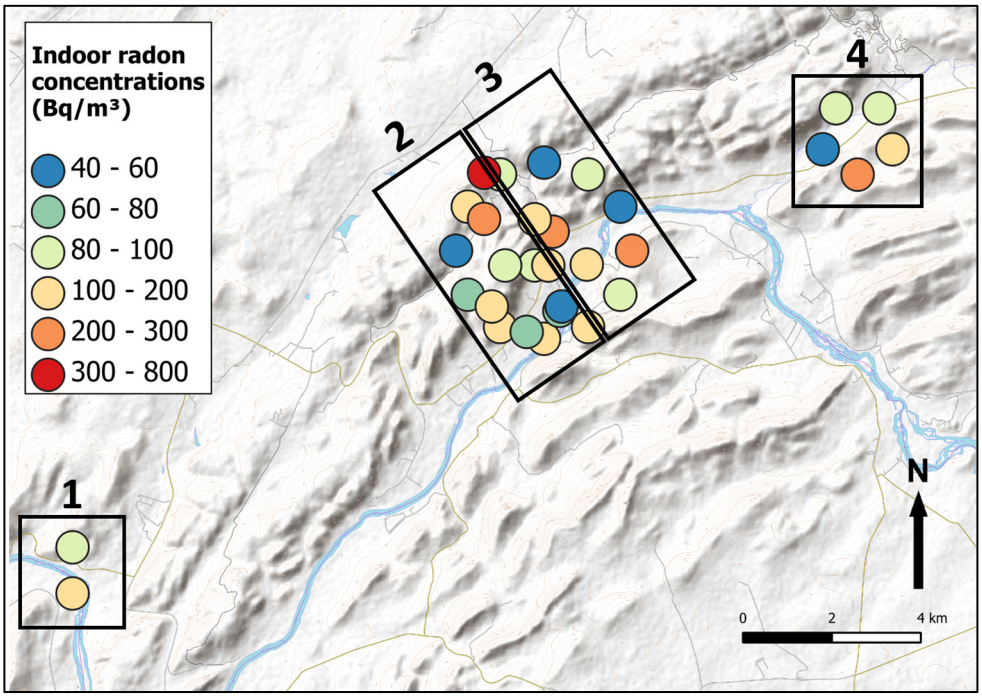

Figure 8. Google terrain map showing the location and indoor radon concentrations measured on the four farms, indicated by the numbered regions, in the Vredefort Dome.

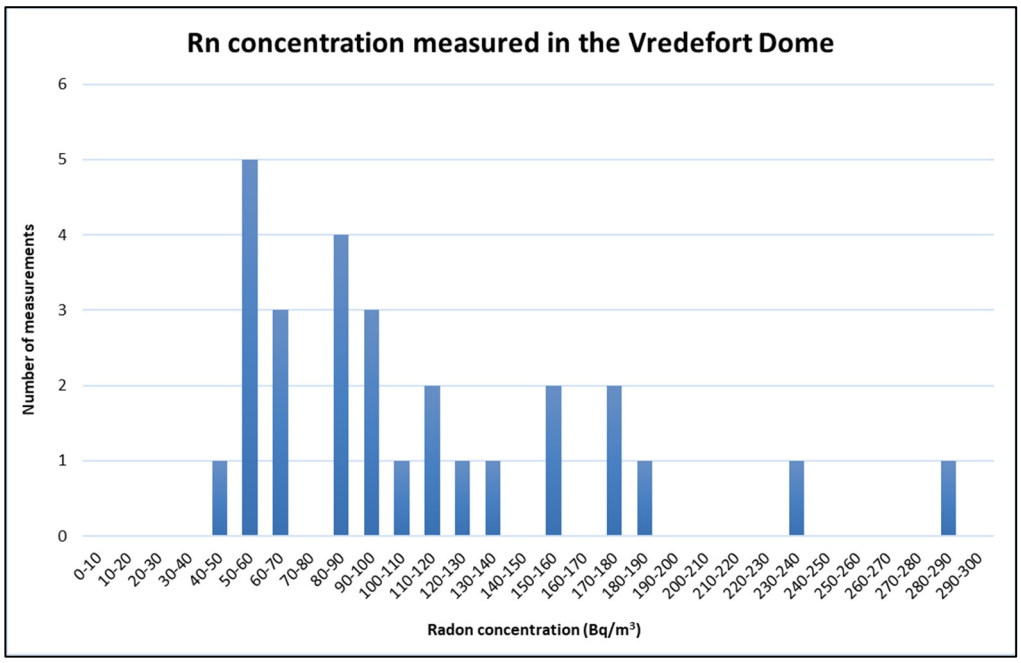

Figure 9. Histogram of the indoor radon concentrations measured on four guest farms in the Vredefort Dome.

Table 1 also compares the average radon concentrations measured in the four farms. As can be seen, similar radon concentrations were found despite the differences in location, construction, and lifestyles of occupants. For comparison, the radon concentrations measured in the mines are also listed in the table, with the location of the mines and where the ground samples were taken indicated in Figure 10.

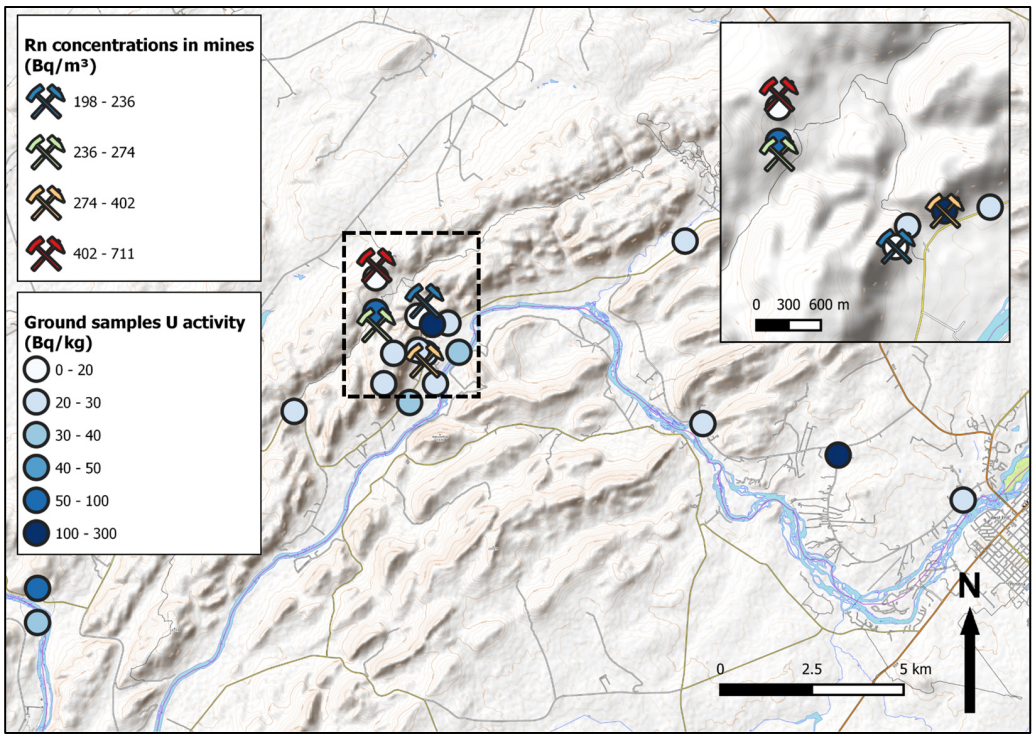

Figure 10. A Google terrain map showing the locations where the ground samples were taken, along with their uranium activity. The locations of the mines and the measured radon concentration are also shown. The inlay shows an enlarged view of the mining area.

Bezuidenhout [5,6] used the mineral content of the surficial geology and a model accounting for radon emanation and exhalation to estimate indoor radon levels for the Vredefort Dome. According to his estimations, indoor radon concentrations between 300 and 1060 Bq/m^3 were to be expected in this area. Considering the statistical distribution of the measured indoor radon concentrations, a lognormal distribution is shown in Figure 11, compared to a normalized normal distribution with a mean of 4.6 and a standard deviation of 0.49. A light skewness towards the right can be observed and using the Jarque–Bera test [34], a *p*-value of 0.014 is obtained. Various studies of indoor radon concentrations have found that the radon distribution in homes situated over a single geological unit with a consistent source of radon in the ground will closely conform to a lognormal distribution [35,36]. However, excessively high, or excessively low, radon concentrations can cause deviation from lognormality [37]. Deviations from lognormality can also be expected due to the variability of the three contributing factors to indoor radon: subsoil under the house, radon from building materials, and radon from outdoors [38], which could explain the lower-than-predicted indoor radon concentrations in the Vredefort Crater.

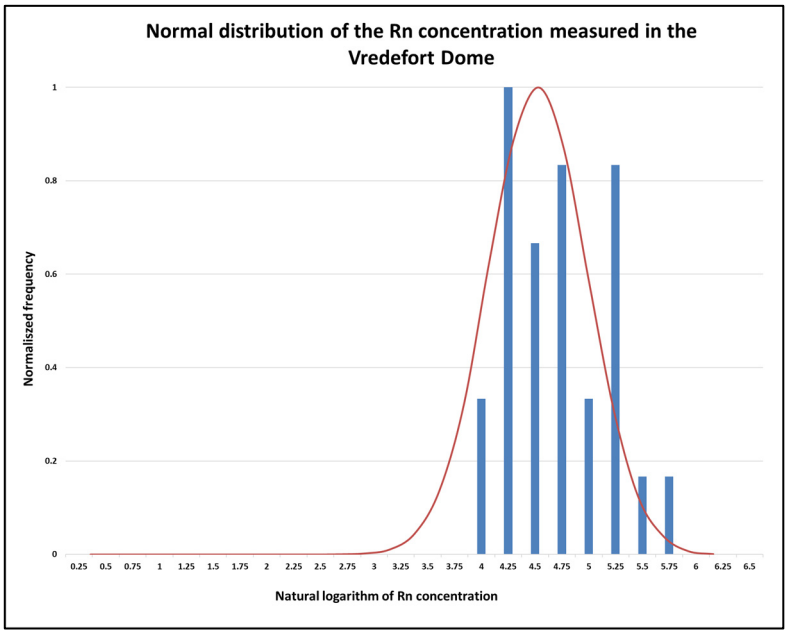

Figure 11. The natural logarithm of the indoor radon concentrations measured in the Vredefort Dome (indicated by the bar graph) compared to a normalized normal distribution with a mean of 4.6 and a standard deviation of 0.49 (indicated by the solid line).

While the in situ measurements showed higher than average uranium concentrations, the uranium activity found in the ground samples averaged 30 Bq/kg, which is on par with the world average of 35 Bq/kg [39]. This lower-than-expected activity might be due to the surficial deposits containing sediments from the Vaal River flowing through the crater that are lower in natural radioactivity. The Turffontein subgroup area of the crater nonetheless showed high radon potential with radon concentrations measured in the mine tunnels averaging 364 Bq/m^3, with the highest measurement being 710 Bq/m^3. As indicated in Figure 9, the ground samples taken near these mines also showed elevated uranium levels. A similar trend was observed in Figure 6, indicating elevated levels of uranium where these mines are located. Thus, it is evident that even though the geology of the Vredefort Crater has high indoor radon potential, corroborating Bezuidenhout's predictions, the emanated gas does not accumulate indoors.

Several studies on indoor radon in South Africa have highlighted that the warm climate, coupled with ventilation and open lifestyles, mitigates the accumulation of radon indoors [40,41]. However, the results found in this study do not align with these obser-

vations. Given that assessments on one of the farms were conducted without occupants, the ventilation in the structures was minimal. High radon concentrations are therefore expected, but due to the location and architecture of the buildings, lower concentrations were measured. Most of the buildings on the farms are built in the Johannesburg subgroup geological formation. As illustrated in Figure 8, the indoor radon measurements were, therefore, concentrated in this region. As shown in Figure 6, this area was found to have lower uranium activities than the Turffontein subgroup. Many of the measured chalets were also constructed on stilts as a precautionary measure against water damage from the Vaal River. Elevation minimizes the risk of radon accumulation, as radon, being a dense gas, tends to accumulate in lower-lying areas. Consequently, lower-than-expected average indoor radon concentrations were measured, despite the high radon potential from the geology.

6. Conclusions

Despite predictions that the geology of the Vredefort Crater would yield elevated indoor radon levels, this proved not to be the case. Though in situ measurements in the three rings of the crater showed elevated concentrations of thorium and uranium, measurements of its radon progeny indoors yielded lower-than-expected concentrations. This is despite these measurements being conducted during colder months and shortly after the COVID-19 pandemic, conditions that would typically lead to elevated levels due to reduced ventilation in the dwellings.

Laboratory analysis of ground samples taken around the measurement area showed uranium activities on par with the global average. However, radon measurements taken among the geology in defunct mining tunnels correlated with Bezuidenhout's predicted indoor radon concentrations. This also correlated with the in situ measurements which showed elevated levels of natural radionuclides in the Turffontein subgroup found in the outer rings of the Vredefort Crater.

This indicates that, despite the geology of the bedrock having high radon potential, this does not translate to elevated concentrations indoors. This was attributed to the location of the buildings in which indoor radon measurements were taken. These buildings are primarily constructed on the Johannesburg subgroup geological formation, which was found to have lower activities of natural radionuclides. This translates to lower indoor radon concentrations, despite the outer rings of the crater showing high radon potential. The net result is average indoor radon concentrations below the World Health Organization (WHO)'s mitigation level of 200 Bq/m^3. It, therefore, poses no hazard to occupants in the dwellings located in the Vredefort Crater.

Author Contributions: Conceptualization, J.B.; methodology, J.B. and R.L.R.; validation, J.B. and R.L.R.; formal analysis, J.B. and R.L.R.; investigation, J.B. and R.L.R.; resources, J.B. and R.L.R.; data curation, J.B. and R.L.R.; writing—original draft preparation, J.B. and R.L.R.; writing—review and editing, J.B. and R.L.R.; visualization, J.B. and R.L.R. All authors have read and agreed to the published version of the manuscript.

Funding: The indoor radon measurement for this research was funded by the Centre for Nuclear Safety and Security (South Africa), project no. CNSS0117-D2-SUN.

Institutional Review Board Statement: Not applicable.

Informed Consent Statement: Not applicable.

Data Availability Statement: Data available on request.

Acknowledgments: Thank you to the owners of the guest farms for allowing measurements to be done on their premises.

Conflicts of Interest: The authors declare no conflict of interest.

References

1. Zeeb, H.; Shannoun, F.; World Health Organization. *WHO Handbook on Indoor Radon: A Public Health Perspective*; World Health Organization: Geneva, Switzerland, 2009.
2. Dubois, G. *An Overview of Radon Surveys in Europe*; European Commission: Luxembourg, 2005.
3. Pantelić, G.; Čeliković, I.; Živanović, M.; Vukanac, I.; Nikolić, J.K.; Cinelli, G.; Gruber, V. Qualitative overview of indoor radon surveys in Europe. *J. Environ. Radioact.* **2019**, *204*, 163–174. [CrossRef] [PubMed]
4. Műllerová, M.; Kozak, K.; Kovács, T.; Smetanová, I.; Csordás, A.; Grzadziel, D.; Holý, K.; Mazur, J.; Moravcsík, A.; Neznal, M.; et al. Indoor radon survey in Visegrad countries. *Appl. Radiat. Isot.* **2016**, *110*, 124–128. [CrossRef] [PubMed]
5. Bezuidenhout, J. Estimating geothermal and background radiation hotspots from primordial radionuclide concentrations in geology of South Africa. *J. Environ. Radioact.* **2023**, *259–260*, 107118. [CrossRef]
6. Smit, H.A.; Bezuidenhout, J. Geology and climate: A novel method to estimate indoor radon exposure risk in South Africa. *S. Afr. Geogr. J.* **2023**, *31*, 1–4. [CrossRef]
7. Bezuidenhout, J. Estimating indoor radon concentrations based on the uranium content of geological units in South Africa. *J. Environ. Radioact.* **2021**, *234*, 106647. [CrossRef] [PubMed]
8. Yuan, Y.; Morishima, H.; Shen, T.; Koga, T.; Wei, L.; Sugahara, T. Measurements of Rn-222, Rn-220 and their decay products in the environmental air of the high background radiation areas in Yangjiang, China. *J. Radiat. Res.* **2000**, *41*, 25–30. [CrossRef] [PubMed]
9. Bisschoff, A.A. The history and origin of the Vredefort Dome. *S. Afr. J. Sci.* **1988**, *84*, 413.
10. Reimold, W.U.; Gibson, R.L. Geology and evolution of the Vredefort impact structure, South Africa. *J. Afr. Earth Sci.* **1996**, *23*, 125–162. [CrossRef]
11. Reimold, W.U. A review of the geology of and deformation related to the Vredefort Structure, South Africa. *J. Geol. Educ.* **1993**, *41*, 106–117. [CrossRef]
12. Reimold, W.U.; Hauser, N.; Oliveira, A.L.; Maciel, A.R.; Goderis, S.; Pittarello, L.; Wegner, W.; Fischer-Goedde, M.; Koeberl, C.; Debaille, V. Genesis of the mafic impact melt rock in the northwest sector of the Vredefort Dome, South Africa. *Meteorit. Planet. Sci.* **2023**, *58*, 907–944. [CrossRef]
13. Fagereng, Å.; Harris, C.; La Grange, M.; Stevens, G. Stable isotope study of the Archaean rocks of the Vredefort impact structure, central Kaapvaal Craton, South Africa. *Contrib. Mineral. Petrol.* **2008**, *155*, 63–78. [CrossRef]
14. Ivanov, B.A. Numerical Modelling of the Largest Terrestrial Meteorite Craters. *Sol. Syst. Res.* **2005**, *39*, 381–409. [CrossRef]
15. Schreyer, W. Metamorphism and fluid inclusions in the basement of the Vredefort dome, South Africa: Guidelines to the origin of the structure. *J. Petrol.* **1983**, *24*, 26–47. [CrossRef]
16. Henkel, H.; Reimold, W.U. Integrated geophysical modelling of a giant, complex impact structure: Anatomy of the Vredefort Structure, South Africa. *Tectonophysics* **1998**, *287*, 1–20. [CrossRef]
17. Hart, R.J.; Andreoli, M.A.G.; Tredoux, M.; De Wit, M.J. Geochemistry across an exposed section of Archaean crust at Vredefort, South Africa: With implications for mid-crustal discontinuities. *Chem. Geol.* **1990**, *82*, 21–50. [CrossRef]
18. Engels, B.; Koch, P.; Badman, T. *Serial Natural World Heritage Properties 2009-064*; IUCN (International Union for Conservation of Nature): Gland, Switzerland, 2009.
19. Meisenberg, O.; Gierl, S.; Tschiersch, J. Measurement of thoron and its progeny in traditional and modern earthen buildings in Germany-methodology and results. In Proceedings of the 2013 International Radon Symposium of the American Association of Radon Scientists and Technologists, Springfield, IL, USA, 22–25 September 2013; Available online: https://aarst.org/symposium-proceedings/ (accessed on 1 October 2023).
20. Reimold, W.U.; Gibson, R.L. The melt rocks of the Vredefort impact structure–Vredefort Granophyre and pseudotachylitic breccias: Implications for impact cratering and the evolution of the Witwatersrand Basin. *Geochemistry* **2006**, *66*, 1–35. [CrossRef]
21. Lana, C. Geology and geochemistry of a granite-greenstone association in the southeastern Vredefort dome, South Africa. *S. Afr. J. Geol.* **2003**, *106*, 291–314. [CrossRef]
22. Reimold, W.U.; Gibson, R.L. *Meteorite Impact! The Danger from Space and South Africa's Mega-Impact the Vredefort Structure*; Chris van Rensburg Publications (Pty) Ltd.: Melville, South Africa, 2005.
23. Bisschoff, A.A. The dioritic rocks of the Vredefort Dome. *Trans. Geol. Soc. S. Afr.* **1972**, *75*, 31–45.
24. Molezzi, M.G.; Hein, K.A.A.; Manzi, M.S.D. Mesoarchaean-Palaeoproterozoic crustal-scale tectonics of the central Witwatersrand basin-Interpretation from 2D seismic data and 3D geological modelling. *Tectonophysics* **2019**, *761*, 65–85. [CrossRef]
25. Bezuidenhout, J. In situ gamma ray measurements of radionuclides at a disused phosphate mine on the West Coast of South Africa. *J. Environ. Radioact.* **2015**, *150*, 1–8. [CrossRef]
26. Bezuidenhout, J. The Testing and Implementation of a Transportable and Robust Radio-element Mapping System. *S. Afr. J. Sci.* **2015**, *111*, 1–7. [CrossRef]
27. Bezuidenhout, J. Measuring naturally occurring uranium in soil and minerals by analysing the 352 keV gamma-ray peak of ^{214}Pb using a NaI(Tl)-detector. *J. Appl. Radiat. Isot.* **2013**, *80*, 1–6. [CrossRef] [PubMed]
28. Kotrappa, P.; Dempsey, J.C.; Ramsey, R.W.; Stieff, L.R. A practical E-PERM (electret passive environmental radon monitor) system for indoor 222Rn measurement. *Health Phys.* **1990**, *58*, 461–467. [CrossRef] [PubMed]
29. Shahbazi-Gahrouei, D.; Setayandeh, S.; Gholami, M. A review on natural background radiation. *Adv. Biomed. Res.* **2013**, *2*, 65. [CrossRef]

30. Mellor, E.T. *The geology of the Witwatersrand: An Explanation of the Geological Map of the Witwatersrand Goldfield*; Government Printing and Stationery Office: Pretoria, South Africa, 1917.
31. Nel, L.T. The geology of the country around Vredefort. *Spec. Publ. Geol. Surv. S. Afr.* **1927**, *6*, 134.
32. Holland, M.J.; Stanistreet, I.G.; McCarthy, T.S. Tectonic control on the deposition of the Turffontein Subgroup around the Vredefort Dome. *S. Afr. J. Geol.* **1990**, *93*, 158–168.
33. World Health Organization. *International Radon Project: Survey on Radon Guidelines, Programmes and Activities (No. WHO/HSE/RAD/07.01)*; WHO: Geneva, Switzerland, 2007.
34. Jarque, C.M.; Bera, A.K. Efficient tests for normality, homoscedasticity and serial independence of regression residuals. *Econ. Lett.* **1980**, *6*, 255–259. [CrossRef]
35. Miles, J.C.H. Mapping the proportion of the housing stock exceeding a radon reference level. *Radiat. Prot. Dosim.* **1994**, *56*, 207–210. [CrossRef]
36. Nero, A.V.; Schwehr, M.B.; Nazaroff, W.W.; Revzan, K.L. Distribution of airborne radon-222 concentrations in US homes. *Science* **1986**, *234*, 992–997. [CrossRef]
37. Daraktchieva, Z.; Miles, J.C.H.; McColl, N. Radon, the lognormal distribution and deviation from it. *J. Radiol. Prot.* **2014**, *34*, 183. [CrossRef]
38. Cinelli, G.; Tondeur, F. Log-normality of indoor radon data in the Walloon region of Belgium. *J. Environ. Radioact.* **2015**, *143*, 100–109. [CrossRef] [PubMed]
39. UNSCEAR. *Sources and Effects of Ionizing Radiation, Annex B: Exposures from Natural Sources*; United Nations Publications: New York, NY, USA, 2000.
40. Le Roux, R.R.; Bezuidenhout, J.; Smit, H.A. The influence of different types of granite on indoor radon concentrations of dwellings in the South African West Coast Peninsula. *J. Radiat. Res. Appl. Sci.* **2019**, *12*, 375–382. [CrossRef]
41. Le Roux, R.; Bezuidenhout, J.; Smit, H. Indoor radon measurements for the South African West coast peninsula. *Radiat. Prot. Dosim.* **2020**, *191*, 144–149. [CrossRef] [PubMed]